A&A 486, 721–734 (2008)
DOI: 10.1051/0004-6361:20079199

Astronomy & Astrophysics

INTEGRAL observations of the blazar Mrk 421 in outburst

Results of a multi-wavelength campaign

G. G. Lichti[1], E. Bottacini[1], M. Ajello[1], P. Charlot[2], W. Collmar[1], A. Falcone[3], D. Horan[4], S. Huber[5], A. von Kienlin[1], A. Lähteenmäki[6], E. Lindfors[6,7], D. Morris[3], K. Nilsson[7], D. Petry[1], M. Rüger[5], A. Sillanpää[7], F. Spanier[5], and M. Tornikoski[6]

[1] Max-Planck-Institut für extraterrestrische Physik, Giessenbachstrasse, 85748 Garching, Germany
e-mail: grl@mpe.mpg.de
[2] Laboratoire d'Astrophysique de Bordeaux, Université Bordeaux 1, CNRS, BP 89, 33270 Floirac, France
[3] Pennsylvania State University, Department of Astronomy & Astrophysics, University Park, PA 16802, USA
[4] High-Energy Physics Division, Argonne National Laboratory, Argonne, USA
[5] Universität Würzburg, Lehrstuhl für Astronomie, Am Hubland, 97074 Würzburg, Germany
[6] Metsähovi Radio Observatory, Helsinki University of Technology TKK, Kylmäläntie 114, 02540 Kylmälä, Finland
[7] Tuorla Observatory, Väisäläntie 20, 21500 Piikkiö, Finland

Received 5 December 2007 / Accepted 3 March 2008

ABSTRACT

Context. If one wants to understand the physics of blazars, better simultaneous observations are important at all wavelengths, so it was fortunate that a ToO observation of the TeV-emitting blazar Mrk 421 with INTEGRAL could be triggered in June 2006 by an increase in the RXTE count rate to more than 30 mCrab. The source was then observed with all INTEGRAL instruments, with the exception of the spectrometer SPI, for a total exposure of 829 ks. During this time several outbursts were observed by IBIS and JEM-X. Multiwavelength observations were immediately triggered, and the source was observed at radio, optical, and X-ray wavelengths up to TeV energies.

Aims. The data obtained during these observations were analysed with respect to time variability, time lags, correlated variability, and spectral evolution and then compiled in a νF_ν spectrum.

Methods. The observations of the different instruments/telescopes were analysed with the usual correlation and time-analysis methods. The spectral analysis of the X-ray data was performed with XSPEC.

Results. Four strong flares at X-rays were observed that were not seen at other wavelengths (partially because of missing data). From the fastest rise in the X-rays, an upper limit could be derived to the extension of the emission region. A time lag between high-energy and low-energy X-rays was observed, which allowed an estimation of the magnetic-field strength. The spectral analysis of the X-rays revealed a slight spectral hardening of the low-energy (3−∼43 keV) spectral index. The hardness-ratio analysis of the Swift-XRT (0.2−10 keV) data indicated a small correlation with the intensity; i.e., a hard-to-soft evolution was observed. At the energies of IBIS/ISGRI (20−150 keV), such correlations are less obvious. A multiwavelength spectrum was composed and the X-ray luminosities were calculated.

Conclusions. The observed flaring activity of Mrk 421 is mainly visible at X-rays. It is found that the spectral change with intensity is small. But at least one flare showed a completely different spectral behaviour than the other flares, so one can conclude that each blob of relativistic-moving electrons has its own individual physical environment that leads to different emission characteristics. From a fit of a leptonic emission model to the data, one finds that the observed variability may be due to a varying efficiency of particle acceleration.

Key words. gamma rays: observations – galaxies: active – galaxies: BL Lacertae objects: individual: Mrk 421

1. Introduction

In 1992 the first AGN, Mrk 421, was detected at energies >500 GeV (Punch et al. 1992). Since then, 20 detections of AGNs have been reported at TeV energies (Blazejowski et al. 2005; Padovani et al. 2007; Wagner 2007). Seventeen of these objects belong to the HBL Lac type of AGNs. They are radio-loud sources with the radio emission originating mainly in a core region and they are characterised by a high polarization at radio and optical wavelengths and a strong variability at all wavelengths. The spectral characteristics point to non-thermal emission processes that presumably take place in a narrow relativistic jet pointed at a small angle to the line of sight. The spectral energy-density distribution of these sources shows two smooth broadband emission components: a first one that reaches a broad peak in the IR to X-ray region and a second one at GeV to TeV energies. Both emission components are clearly separated (see Fig. 3 of Ghisellini et al. 1996).

It is believed by many researchers that both components are generated by the same leptonic population (electrons and/or positrons) moving at relativistic speed in the jet (Blandford & Rees 1978), which creates the low-energy photons via incoherent synchrotron radiation and the high-energy gamma-rays via inverse-Compton scattering of soft photons. This common origin would explain the similarity of the two components (Ghisellini & Maraschi 1996); hence, a similar temporal evolution is expected for both components if this scenario is correct. Such time correlations were indeed observed by observations at X-ray

and TeV energies (Buckley et al. 1996; Catanese et al. 1997; Fossati et al. 2008), and they even extend to the optical and radio wavelengths (Katarzynski et al. 2003). This idea is further supported by the observed polarization at radio wavelengths (Piner & Edwards 2005). However, there are some exceptions to these clear correlations, such as the orphan TeV flares reported by Blazejowski et al. (2005) and Krawczynski et al. (2004). Unfortunately, measurements between 10 keV and 1 GeV that would allow us to further constrain this common origin have been scarce. Until now only few measurements between 10 keV and 1 GeV exist. COMPTEL has detected Mrk 421 in the 10−30 MeV range with 3.2σ (Collmar et al. 1999). EGRET, however, has detected this source many times above 100 MeV (Hartman et al. 1999).

Since the high-energy emission is not as well understood, many different models try to explain this emission component. In one scenario the low-energy synchrotron photons are boosted to high energies by the same electron population that creates the synchrotron photons (the synchrotron self-Compton (SSC) models, Königl 1981; Maraschi et al. 1999; Bloom & Marscher 1996). Although this process must be at work in all blazars and if the synchrotron-emission hypothesis is correct, it may not be the dominant one. In another model the seed photons for the inverse-Compton effect enter from outside the jet region, e.g. from the accretion disc or from clouds surrounding the jet (Dermer et al. 1992; Sikora et al. 1994). Apart from these lepton models, the so-called hadron models were proposed in which the high-energy γ-rays are produced by proton-initiated cascades (Mannheim 1993; Mücke & Protheroe 2000) and/or proto-synchrotron emission (Aharonian 2000; Mücke et al. 2003).

The homogeneous SSC model makes very definite predictions about the correlated behaviour of the high-energy end of both the synchrotron and SSC components: simultaneous variability of photons and well-defined correlated spectral changes in the medium/hard X-rays and TeV bands. But these models have problems with the bulk-Lorentz factor statistics (Henri & Saugé 2006) and it seems to be very important to measure a detailed variability pattern from X-rays up to TeV γ-rays. Several alternatives have been proposed, and each needs to be quantified in more detail. However, in general one can say that in the leptonic models synchrotron radiation is "primary" and inverse Compton radiation "secondary", while for at least one hadronic model it is the opposite: the γ-rays are produced by the "primary" protons through cascades, while the X-rays have a synchrotron origin in the "primary" electrons. In this case the relation between the two components can be looser than for lepton models. Also, in this case the "cascade" spectra are quite soft (lots of soft γ-rays).

To investigate all these theoretical ideas and models, an INTEGRAL ToO proposal was submitted to observe the blazar Mrk 421 when it becomes active. Mrk 421 has a redshift of 0.031, and with a distance of about 125 Mpc (for H_0 = 71 km/(s Mpc)) is one of the closest and therefore brightest blazars. It hosts a supermassive black hole with a mass of $(2-8) \times 10^8\ M_\odot$ in its centre (Barth et al. 2003; Falomo et al. 2002; Treves et al. 2003). At high energies, Mrk 421 has been detected in the 10−30 MeV range by COMPTEL with 3.2σ (Collmar et al. 1999) and many times above 100 MeV by EGRET (Hartman et al. 1999) and in the TeV range by Cherenkov telescopes (Kerrick et al. 1995; Aharonian et al. 1999; Sambruna et al. 2000; Krennrich et al. 2001; Aharonian et al. 2005; and Rebillot et al. 2006). In June 2006, Mrk 421 became active and our INTEGRAL proposal was activated. The proposal foresaw not only observations with the INTEGRAL instruments but also observations with other telescopes at all wavelengths. Data at radio, optical, X-ray, and TeV wavelengths were taken.

However, the observations at TeV energies turned out to be sparse because the visibility period for the Cherenkov telescopes approached its end. It was thus impossible to investigate possible correlations or time lags between the synchrotron and inverse-Compton emission as we wished. We therefore had to concentrate our analysis mainly on the INTEGRAL data itself and on the multi-wavelength spectrum. Preliminary results of this analysis have been already published by Lichti et al. (2007).

2. Observations

In April 2006 the blazar Mrk 421 increased its intensity to a level >30 mCrab as measured by the all-sky monitor (ASM) of RXTE (the quiescent intensity fluctuates strongly around an average value of 10−15 mCrab). It remained at this level until September 2006. This triggered an INTEGRAL observation and correlated multiwavelength observations in the radio, optical, X-ray and TeV ranges. The details of the various observations are given in this section.

2.1. INTEGRAL observations

On June 14, 2006 (MJD 53900) at 09:53:16.8 h UT, an observation of this source was triggered with INTEGRAL. The observation lasted about nine days and ended on June 26, 2006 (MJD 53911) at 02:03:55.4 h UT. In total the source was observed for 829 ks with the instruments IBIS, JEM-X, and OMC in pointing mode (the spectrometer SPI was disabled because of annealing its Ge detectors).

The data of the three operating instruments were analysed with the INTEGRAL Off-line Scientific Analysis (OSA) software version 5.1 using the latest response matrices available for that software. The collected data were screened by computing the median count rate for each science window, and it was then compared with each of the other science windows and their distributions. Those science windows showing rates higher than 10 standard deviations from the median count rate were checked again. By this screening effort, three suspicious science windows were detected. A closer look revealed that these science windows belonged to times when INTEGRAL was close to the radiation belts and that the high counting rates were due to the trapped charged particles. After this screening process, 230 science windows remained and were considered for further analysis.

Mrk 421 was clearly detected by all three INTEGRAL instruments. In Fig. 1 IBIS/ISGRI, JEM-X, and OMC skymaps in galactic coordinates are shown. In all three maps the source is detected at a high significance level [by IBIS in the energy interval 20−40 keV with 160σ, by JEM-X in the energy interval 3−4.5 keV with 720σ, and by OMC (limiting magnitude ≈18) with $m_v \approx 12.87$]. It should be mentioned that in the field of view of IBIS another AGN, NGC 4151, was observeded, which was detected in the energy intervals 20−50 keV, 50−100 keV, and 100−150 keV with 34.7σ, 15.1σ, and 5.4σ, respectively.

The magnitudes m of OMC were converted into differential flux values with the following formula (obtained from A. D. Garau of the OMC team)

$$S\left[\frac{\text{erg}}{\text{cm}^2\ \text{s}\ \text{Å}}\right] = 3.64 \times 10^{-9} \times 10^{-0.4m} \quad (1)$$

$$\Delta S = 0.921 \cdot S \cdot \Delta m. \quad (2)$$

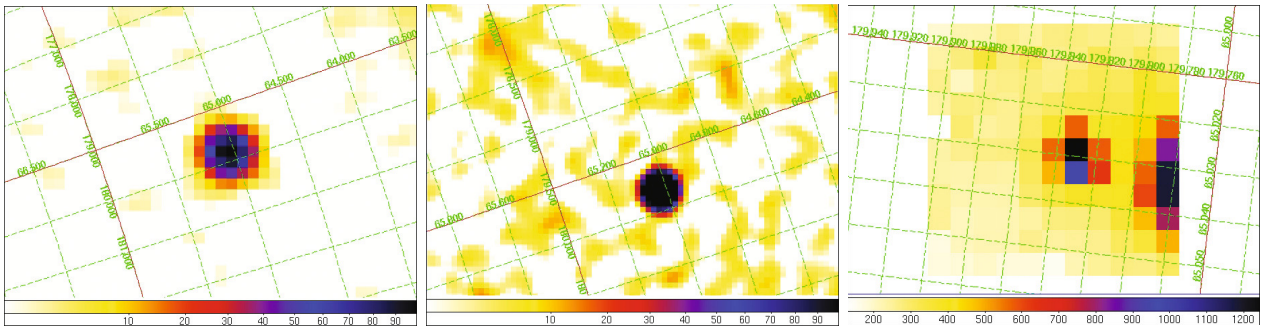

Fig. 1. IBIS/ISGRI, JEM-X, and OMC skymaps (*from left to right*) of the region around Mrk 421 for 20−40 and 3−4.5 keV and at visible wavelengths, respectively, in galactic coordinates. In the OMC map, the bright star 51 Uma ($V = 6$), which is clearly separated from Mrk 421 (distance ∼2 arcmin), is seen at the edge of the field of view.

The calibration of (1) was obtained from the flux of a star with $m = 0$ at 5500 Å from Wamsteker (1981). The contribution of the host galaxy was estimated from the colour of a typical elliptical galaxy ($V - R = 0.6$) and its R-band flux of 16.5 mJy to be 9.5 mJy. This host-galaxy flux was taken into account when calculating the energy-density flux. A correction for a possible contribution from the bright ($V = 6$) close-by (∼2 arcmin away) star 51 Uma (HR 4309) is not necessary because of the sharp point-spread function of the OMC, which drops practically to zero at a distance of 2 arcmin (attenuation factor $<10^{-23}$).

Immediately after the beginning of the observation with INTEGRAL, the other observers participating in this multiwavelength campaign were alerted, and they commenced with their observations as allowed by the observational constraints.

2.2. VLBA observations

Following the notification of the INTEGRAL observations, a request to trigger our previously-approved target of opportunity VLBA observations was sent to NRAO on June 13, 2006. After preparation of the observing schedule, the project entered the queue for dynamical scheduling at the VLBA and actually got scheduled on June 25. The observations started at 17:00 UT on that day and lasted for 14 h, with scans alternated on six different frequency bands (2.3, 5.0, 8.4, 15.4, 22.2, and 43.2 GHz). The total observing time on each frequency band was roughly 1 h at 2.3, 5 and 8.4 GHz, 2 h at 15 GHz, 3 h at 22 GHz, and 6 h at 43 GHz. Additional scans on calibrator sources were also inserted into the schedule for proper amplitude and polarization calibration.

After correlation at the Array Operation Center in Socorro, the data were calibrated and corrected for residual delay and delay rate using the NRAO Astronomical Image Processing System (AIPS) and subsequently imaged using the Caltech VLBI imaging software DIFMAP. The flux density was then integrated over each image to produce the total flux densities used in the present study of the spectral energy distribution of Mrk 421. The values of the flux density derived so far in this way are 0.283 Jy at 5 GHz and 0.273 Jy at 8.4 GHz. Presentation of the VLBI images is deferred to a future paper, which will present and discuss the results of the VLBI data analysis in more details.

2.3. Observations with the Metsähovi radiotelescope

The 37 GHz observations were made with the 13.7 m diameter Metsähovi radio telescope, which is a radome-enclosed paraboloid antenna situated in Finland (24 23′38″E, +60 13′05″). The measurements were made with a 1 GHz-band dual-beam receiver centred at 36.8 GHz. The HEMPT (high-electron mobility pseudomorphic transistor) front end operates at room temperature. The observations are ON−ON observations, alternating the source and the sky in each feed horn. A typical integration time to obtain one flux-density data point is 1200−1400 s. The detection limit of our telescope at 37 GHz is approximately 0.2 Jy under optimal conditions. Data points with a signal-to-noise ratio <4 were handled as non-detections.

The flux-density scale was set by observations of the bright compact HII region DR 21. Sources 3C 84 and 3C 274 were used as secondary calibrators. A detailed description on the data reduction and analysis is given in Teräsranta et al. (1998). The error estimate in the flux density includes the contribution from the measurement rms and the uncertainty of the absolute calibration.

The observations of Mrk 421 during the INTEGRAL campaign were made in varying weather conditions. The first measurements were non-detections, but shortly the flux level increased and several detections were achieved on days 53902 and 53903. The rest of the campaign was lost due to changeable weather and the end of the telescope time allocation.

The sparse radio data do not allow any conclusion by themselves. For the Metsähovi observations Mark 421 stays basically on the verge of the detection limit and it never gets very bright. This is typical of the TeV blazars observed at Metsähovi. However, this kind of behaviour is different from other GeV-peaking gamma-ray blazars, and may reflect the different mechanism for the production of gamma rays in Mrk 421 and the other TeV blazars.

2.4. KVA observations

Mrk 421 was observed in the R-band (centred at 640 nm) with the 35 cm KVA telescope on La Palma, Canary Islands, during 8 nights on June 14−22, 2006. The camera employed was an SBIG ST-8 with a gain factor of 2.3 e^-/ADU and and readout noise of 14 e^-. Each night 4−10 exposures of 180 s were made. The images were processed in a standard way (bias subtraction, dark subtraction and flat-fielding) and the raw counts of Mrk 421 and stars 1−3 in Villata et al. (1998) were integrated within a 15 arcsec diameter aperture. The magnitude of Mrk 421 was determined by comparing its counts to star 1, for which $R = 14.04$ from Villata et al. (1998) was assumed. The use of differential mode effectively eliminates the influence of varying transparency due to clouds, etc., and accurate fluxes can even be

obtained under varying observing conditions. The flux of Mrk 421 was then computed from

$$F[\mathrm{Jy}] = 3080.0 \times 10^{-0.4 \cdot R}, \quad (3)$$

where R is the R-band magnitude (with an effective wavelength of 6400 Å). The normalization constant was taken from Table IV of Bessell (1979). The host galaxy flux with the 15 arcsec diameter aperture is 8.0 ± 0.5 mJy (Nilsson et al. 2007), and this flux was subtracted from the observed fluxes before proceeding with the analysis.

2.5. RXTE observations

The data of the all-sky monitor (ASM) of RXTE (for a description see Levine et al. 1996) monitors the X-ray sky more or less continuously in the energy range 1.5−12 keV. Its data are publicly available. The data for Mrk 421 were downloaded and the fifth lightcurve at the top of Fig. 2 was produced. The RXTE counting rates were translated into energy fluxes by using the Crab-nebula flux from Kirsch et al. (2005). These authors derived an energy flux of 2.2×10^{-8} erg/(cm^2 s) for the Crab for the energy interval 2−10 keV (i. e. the energy range of the ASM). This corresponds to an RXTE counting rate of 73 counts/s, so 1 RXTE count/s corresponds to 3×10^{-10} erg/(cm^2 s). With this value, the RXTE-counting rates were converted to energy fluxes.

2.6. Swift-XRT observations

The X-ray Telescope (XRT) instrument on the Swift Observatory (Burrows et al. 2005; Gehrels et al. 2004) is sensitive to X-rays in the 0.2−10 keV band. These data were reduced using the latest HEAsoft tools (version 6.1.0), including Swift software version 2.0 and the latest response (version 8) and ancillary response files (created using xrtmkarf) available in CALDB at the time of analysis. Data were screened with standard parameters, including the elimination of time periods when the CCD temperature was warmer than −48 °C. Only WT (windowed timing) mode data was used in this analysis due to the high rates of the active source, and only grades 0−2 were included. Since the count rate stayed below ≈100 c/s, the WT mode data is free of significant pile-up effects. These data were corrected for effects due to bad columns and bad pixels. Source and background regions were both chosen in a way that avoids overlap with serendipitous sources in the image. All analysis and fitting of XRT data was done in the 0.3 to 10 keV energy band. Due to the low hydrogen-column density towards Mrk 421 of 1.43×10^{20} cm^{-2}, the absorption is <0.5% and was neglected. Finally the measured counting rates were transformed into energy fluxes using the formula

$$F\left[\frac{\mathrm{erg}}{(\mathrm{cm}^2\ \mathrm{s})}\right] = (4 \pm 2.5) \times 10^{-11} \cdot R_{\mathrm{cts/s}}. \quad (4)$$

This conversion factor was calculated using a subset of these Swift-XRT Mrk 421 observations, which included both high- and low-state flux measurements. For each time period used, the rate was calculated using the analysis described above, and the spectral fits to these data allowed the flux to be calculated, thus resulting in a conversion factor. Since a single conversion factor was used, rather than many individual time-resolved spectral fits, the large error bars are required to represent the variation in this conversion factor due to spectral variability of the source.

2.7. Swift-BAT observations

The Burst-Alert Telescope (BAT, Barthelmy et al. 2005) on board the Swift satellite mission (Gehrels et al. 2004) is a coded-mask telescope sensitive to the 15−200 keV energy range. Thanks to the pointing strategy and to its wide field of view (FoV), BAT surveys ~80% of the sky every day. We thus looked in the archive for BAT observations that contained Mrk 421 in the FoV. We selected all observations included in the time-span June 12−26, 2006. The BAT data were processed using the HEASOFT 6.2 package and according to the recipes presented in http://swift.gsfc.nasa.gov/docs/swift/analysis/threads/bat_threads.html. Spectra and lightcurves were corrected for off-axis variation of the rates and residual background contamination as described in Ajello et al. (2008).

2.8. Whipple observations

The Whipple Telescope is located at the Fred Lawrence Whipple Observatory, at an elevation of 2300 m in Southern Arizona. It comprises a 10 m dish on which 248 mirrors are mounted. These mirrors reflect the Cherenkov light from extensive air showers onto a 379-element imaging camera at the focal plane of the telescope. The instrument is described in detail by Kildea et al. (2007).

The Mrk 421 data presented here were taken in "*tracking*" mode at large zenith angles on June 18, 19, and 21, 2006 (MJD 53904, 53905, and 53907). The observing scans were performed with the gamma-ray source at the centre of the field of view. No separate control data were taken. Rather, the background rate of gamma-ray-like events was estimated from the distribution of events passing all but the orientation image-selection cuts (Horan et al. 2002). The gamma-ray rates are calculated in units of the flux from large zenith-angle observations of the Crab Nebula, the standard candle in TeV astronomy, and are given in Table 1. They were converted into energy-flux values by integrating the Crab spectrum of Hillas et al. (1998) from the threshold energies of 0.6 and 0.9 TeV to infinity and using the resulting flux values as normalization for the time-averaged spectrum of Mrk 421 as given by Aharonian et al. (1999). Under the assumption that the spectral shape is constant this normalization was adapted to the measured flux values.

3. Results of the timing analysis

It is known that blazars are time variable on all different time scales. This is especially true for TeV blazars and thus also for Mrk 421. We have therefore investigated our data in this respect and compare the data collected at different energies with each other and search for possible correlations betweeen them. The results of this exercise are presented in this section.

3.1. The Lightcurves

The lightcurves of the various observations are shown in Figs. 2 to 7. Whereas the sampling of the lightcurves of the three INTEGRAL instruments and the SWIFT-XRT telescope is ample, this is not the case for the other lightcurves. This makes the search for intensity correlations between the different wavebands difficult if not even impossible. Another fact is striking when one looks at the lightcurves. Although four strong flares are seen in the ISGRI lightcurve (and even more in the Swift-XRT lightcurve of Fig. 3), these flares are not visible at the

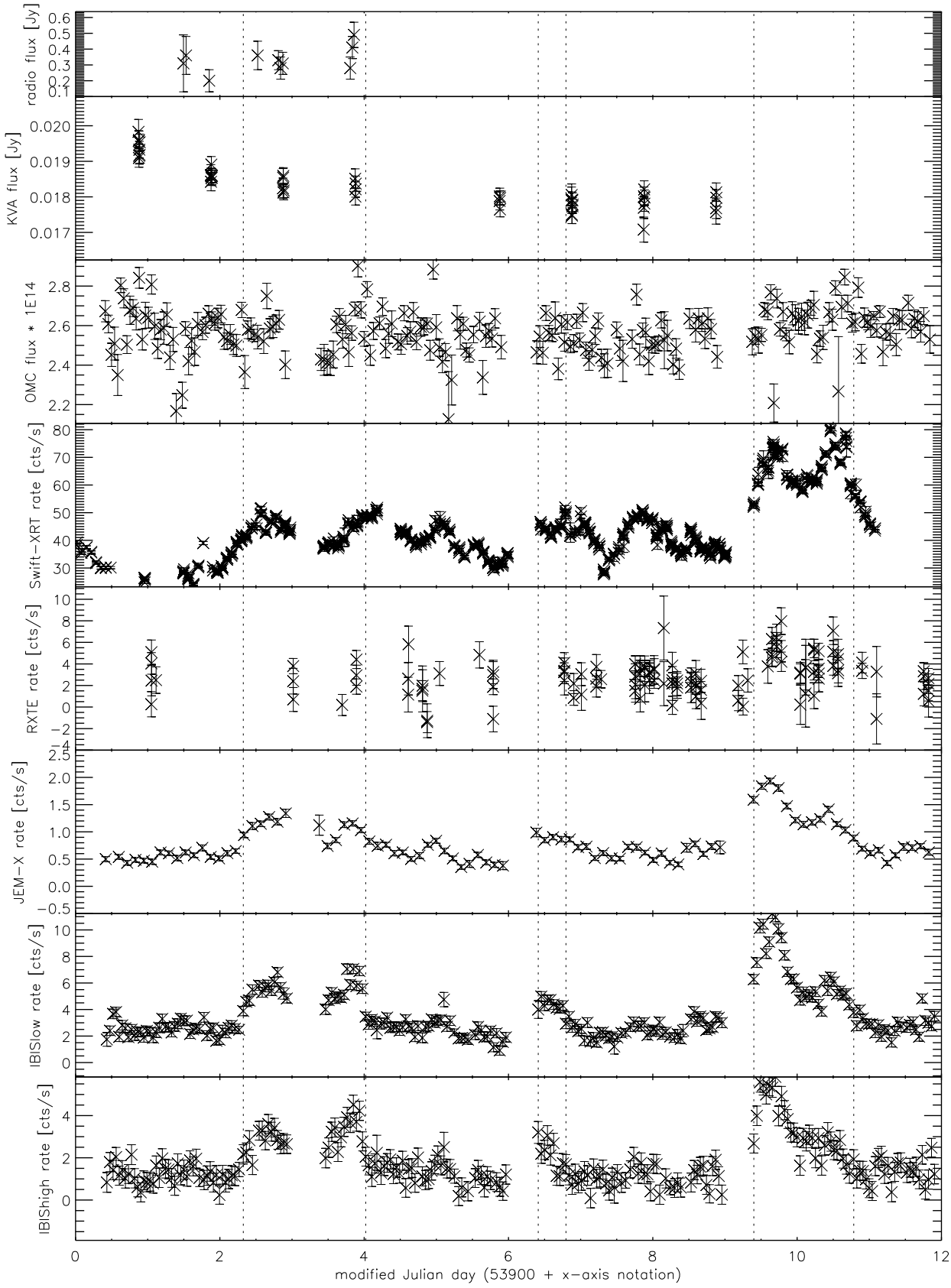

Fig. 2. All lightcurves for Mrk 421 at radio, optical, X-ray, and gamma-ray wavelengths. The data of the OMC (given in erg/(cm^2 s Å)) and KVA telescopes were not extinction-corrected, since the extinction E_{B-V} in the direction of Mrk 421 is only 0.03. The time intervals for the active phases are indicated by the dotted lines.

Table 1. The measured TeV intensities (in Crab units) of Mrk 421 as measured by the Whipple observatory.

MJD[a]	Flux value (Crab units)	Error of flux value	Energy density [erg/(cm^2 s)]	Energy-density error
53904.17	0.25	0.38	2.90×10^{-11}	4.46×10^{-11}
53905.17	1.63	0.42	1.89×10^{-10}	6.31×10^{-11}
53907.20	0.39	0.28	3.71×10^{-11}	2.82×10^{-11}

[a] The integration time for each data point was 28 min. The centre of each time interval is given.

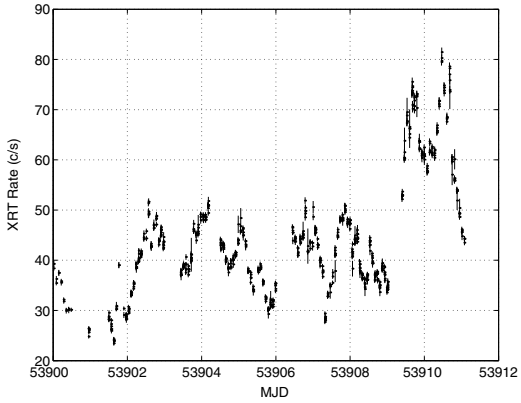

Fig. 3. Swift-XRT lightcurve in the energy interval 0.3−10 keV. The dotted lines give only the coordinates, not the intervals of the active phases as in Figs. 4 to 6.

other energies. An inspection of the X-ray lightcurves reveals the following:

- the strength and the shapes of the flares vary significantly;
- the shape of the flares is not symmetric (some flares show a sharp rise and a slow decay time, others a slow rise and a fast decay time);
- the duration of the flares is about 0.5 days;
- comparing Figs. 3 and 4 one can see that the energy spectrum of the flare around day 53910.5 is qualitatively softer than the spectrum of the other flares;
- from a linear fit to all the data, it becomes obvious that the total intensity is slightly increasing with time.

Especially interesting is that these flares are also not seen by the OMC. It is the common understanding that in blazars, if viewed under small angles, the optical thermal emission of the accretion disk and of the galaxy is outshined by the non-thermal beamed emission of the jet (Tavecchio 2005). Since both the X-rays and the optical photons are produced by the same population of relativistic electrons via synchrotron emission, one would expect similar (if not even identical) lightcurves, if this scenario is correct. For Mrk 421, this happened to be the case in 2001 when a flare showing variability in the visible band coincident with that at radio wavelengths and at TeV energies was observed (Katarzynski et al. 2003). That this is not observed in our data contradicts to this hypothesis and asks for an explanation. Possible explanations will be discussed in the last section.

From the radio, KVA, OMC, and RXTE lightcurves of Fig. 2, the average fluxes/magnitude/counting rates were calculated. The weighted means are given in Table 2. The ISGRI lightcurve of Fig. 5 was used to define by eye the times when the source was in quiescent and active states. Three time intervals were specified and their boundaries are given in Table 3.

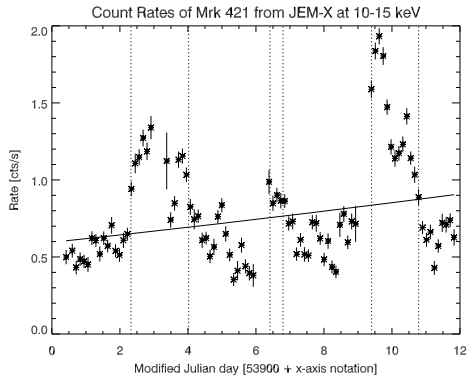

Fig. 4. JEM-X lightcurve in the energy interval 10−15 keV. The time intervals for the active phases are indicated by the dotted lines. A parabola was fitted to all counting rates to guide the eyes.

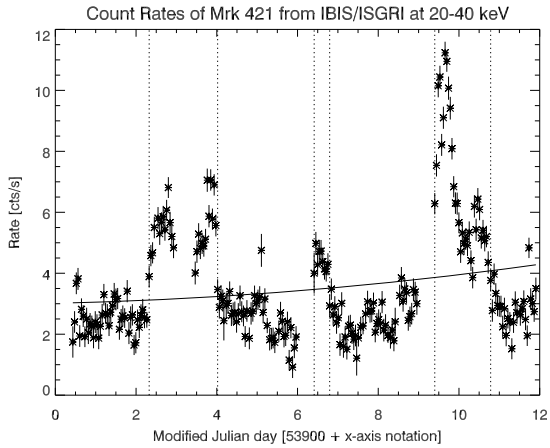

Fig. 5. IBIS/ISGRI lightcurve in the energy interval 20−40 keV. The time intervals for the active phases are indicated by the dotted lines. A parabola was fitted to all counting-rate values to guide the eyes.

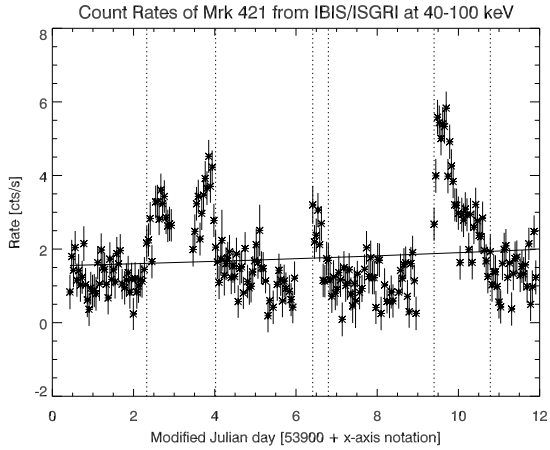

Fig. 6. IBIS/ISGRI lightcurve in the energy interval 40−100 keV. The time intervals for the active phases are indicated by the dotted lines. A parabola was fitted to all counting-rate values to guide the eyes.

3.2. Rise-time analysis

The rise-time scale gives information about the extension of the emission region. From observations at TeV energies it is known that Mrk 421 shows short-time variability with time scales of about one day and shorter (Aharonian et al. 2002, 2003). Doubling times with time scales of about one day or even

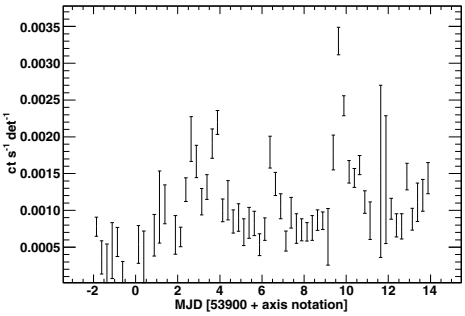

Fig. 7. Swift-BAT lightcurve in the energy interval 15−200 keV.

down to 15−20 min were also reported by Cortina & Schweizer (2002) and Krennrich et al. (2003). In May 1996 two fast flares were observed (Gaidos et al. 1996). The first one had an intensity 10 times higher than the one of the Crab nebula (the highest flux ever observed from this source at these energies) with a time scale of <1 day. The second one a week later had an unprecedented time scale of ∼30 min indicating a very small emission region!

An inspection of the ISGRI ligtcurves reveals that the steepest ascent occurred in the third time interval. Fitting an exponential rise-time law of the form $a \cdot e^{\frac{t}{t_0}}$ to the data of the energy interval 40−100 keV one finds a value of 2.79 h for t_0. In the energy interval 20−40 keV, the increase is somewhat slower (only 4.28 h). One can now calculate the size of the emission region with the formula

$$l \leq \frac{c \cdot t_0 \cdot \delta}{1+z} \tag{5}$$

with c the speed of light, δ the Doppler factor (=12; from Kino et al. 2002) and z the redshift. Inserting the value from above one means that the emission region must be <234 AU (the Schwarzschild radius of Mrk 421 is between 4 and 16 AU and the radius of the last stable orbit between 12 and 47 AU). From the shortest time scale measured at TeV energies an extension was derived of the emission region of ≤2.5 AU (Aharonian et al. 2002). From pure high-resolution radio-interferometric observations Charlot et al. (2006) derived an upper limit on the high-energy emission region of 0.1 pc (≃20 000 AU). Thus a dependence of the size of the emission region on energy seems to exist: the higher the energy, the smaller the emission region!

3.3. Variability analysis

The fractional variability V (see appendix in Fossati et al. 2000, for the definition) was calculated for all lightcurves. The result is shown in Table 4. The same behaviour as already found by previous authors (e.g. Fossati et al. 2000; Sembay et al. 2002) is confirmed by our observations: the fractional variability increases with energy. This behaviour seems to be common in blazars (Ulrich et al. 1997). If we fit a power law to the data we get $V \propto E^{0.28}$. This is in good agreement with the laws found by Fossati et al. (2000) ($V \propto E^{0.25}$) and by Giebels et al. (2007) ($V \propto E^{0.24}$). This reflects that the higher energies are emitted from regions closer to the central black hole, which are smaller in extension than regions farther away. Since the emission from small regions can vary faster than the ones from larger regions the observed trend can be understood qualitatively.

Table 2. Weighted means of the fluxes/magnitude/counting rates in Fig. 2.

Instrument	Average value	Error
radio	0.33 Jy	0.026 Jy
KVA	1.83×10^{-2} Jy	3×10^{-4} Jy
OMC	2.579×10^{-14} erg/(cm^2 s Å)	0.007 erg/(cm^2 s Å)
RXTE	2.86 cts/s	0.3 cts/s

Table 3. Time boundaries in modified Julian Date (days:hours:minutes: seconds) for the active state.

Interval number	Start time	End time
1	53902:07:47:23	53904:00:29:59
2	53906:09:53:24	53906:19:07:15
3	53909:09:36:14	53910:18:49:56

Table 4. The fractional variability measure V for the different lightcurves.

Instrument	Low-energy bound [eV]	High-energy bound [eV]	V
Metsähovi	–	–	undefined
KVA	1.85	2.04	0.0314
OMC	2.14	2.39	0.0393
Swift-XRT	300	10 000	0.266
RXTE	2000	10 000	0.4258
JEM-X	10 000	15 000	0.4266
IBIS/ISGRI	20 000	40 000	0.5146
IBIS/ISGRI	40 000	100 000	0.5723

3.4. Time-lag analysis

The time lag between the two ISGRI lightcurves of the energy intervals 20−40 keV and 40−100 keV was calculated with the Z-transformed discrete-correlation function (ZDCF; Edelson & Krolik 1988; Tal 2007). The value of the ZDCF as a function of the time lag τ is shown in Fig. 8. Five maxima with ZDF values around 0.5 are seen, two at $\tau \approx \pm 3.4$ days, two at $\tau \approx \pm 7$ days, and one at $\tau \approx 0$ day. The shifts at ±3.4 days and ±7 days correspond to the time difference between the flares seen in Figs. 5 and 6 and thus do not reveal new information. Important, however, is the question whether the central peak has its maximum really at $\tau \approx 0$ days. To find this out, a Gaussian and a linear background were fitted to the data from $\tau = -1$ day to $\tau = +1$ day. The data can be described well with a Gaussian ($\chi^2_{\rm red} = 0.114$). The fit to the data reveals that, with a significance of 1.8σ, the maximum is not at a time lag of zero, but at $\tau = (-40.8 \pm 23.3)$ min. The negative sign indicates that the variations at lower energies lag behind those at the high energies.

The same time-lag analysis was performed for the IBIS (20−40 keV) / JEM-X (10−15 keV) and the JEM-X (10−15 keV) / Swift-XRT (0.3−10 keV) lightcurves. In the first case the time lag is consistent with a lag of zero minutes (actually -4.25 ± 30.4 min), and in the second case the time lag is positive and has a value of (102.6 ± 59) min. Similar time lags (35−47 min) were found by Fossati et al. (2000) for the energy ranges 0.1−1.5 keV and 3.5−10 keV using BeppoSAX data and by Takahashi et al. (1996) as a function of energy for the energy range 0.5−7.5 keV using ASCA data. Especially Takahashi et al. (1996) found that the time lags decrease with increasing energy, consistent with our results. But their time lags were all negative, while we also find positive timelags. Positive time lags were also measured by Ravasio et al. (2004) and by

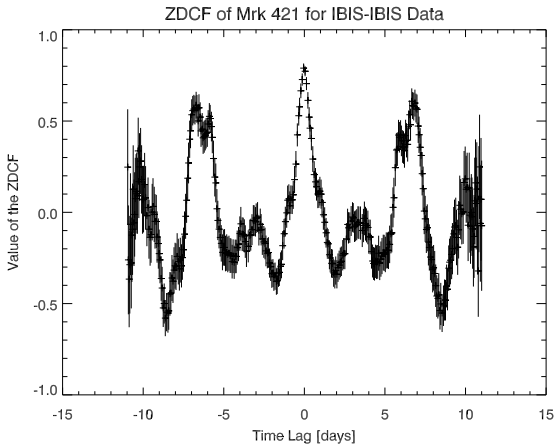

Fig. 8. The Z-discrete correlation function of the IBIS data.

Brinkmann et al. (2005) in the energy range 0.6−10 keV using XMM data. But the statistical significance of our time lags is marginal, so one can question their reality. The importance of this question and the ample number of lightcurves at different energies measured during our multiwavelength campaign would deserve a more detailed analysis, which is, however, not the scope of this paper.

The time lags must be produced by energy-dependent mechanisms, for instance, particle cooling, and acceleration. The higher-energy particles cool faster and accelerate slower than the lower-energy particles, therefore the negative timelag can be used to estimate the magnetic-field strength from the measured negative time lag. The theory of this process was developed by Kazanas et al. 1998. Based on the results of this theory Chiapetti et al. (1999) derived the Eq. (6) which provides an estimate of the magnetic field B:

$$B = 300 \cdot \left(\frac{1+z}{\nu_1 \cdot \delta}\right)^{\frac{1}{3}} \cdot \left(\frac{1-\sqrt{\frac{\nu_1}{\nu_0}}}{\tau}\right)^{\frac{2}{3}} \approx \left(\frac{300^3}{\nu_1 \cdot \delta}\right)^{\frac{1}{3}} \cdot \tau^{-\frac{2}{3}} \quad (6)$$

where δ is the Doppler factor, z the redshift, and ν_0 and ν_1 are the frequencies of the corresponding energy intervals (in units of 10^{17} Hz) at which the time lag τ (τ in s) has been measured.

For determining the frequencies ν_0 and ν_1 the mean energy for the energy intervals given above were calculated using the power laws derived from the fit to the data (see Tables 5 and 6). Inserting those, together with the other parameters from above, one gets a magnetic-field strength of (0.08 ± 0.03) G. Similar values (0.12 G) were found by Kino et al. (2002) using the observables of Mrk 421 from Kataoka (2000), by Konopelko et al. (2003) (0.1 G) and by Giebels et al. (2007) (∼0.1 G).

But the value of the Doppler factor is highly uncertain. Rebillot et al. (2006) investigated two models with $\delta = 50$ and 1000 (in their model a higher Doppler factor corresponds to a smaller emission region). If we adopt these values, we find values of (0.06 ± 0.02) G and (0.02 ± 0.007) G, respectively, for the magnetic-field strength B. Values of the Doppler factor between 50 and 100 seem to be suggested by the data (see Krawczynski et al. 2001; and Mastichiadis & Kirk 1997). However, such large Doppler factors are not observed with VLBI observations (e.g. Piner & Edwards 2005), so this might indicate a velocity structure in the jet (Georganopoulos & Kazanas 2003; Ghisellini et al. 2005).

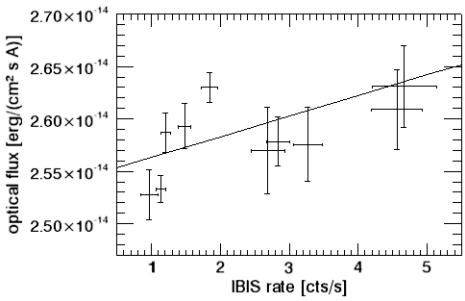

Fig. 9. Intensity correlation between OMC and IBIS data. The count-rate range of the ISGRI count rates was split into arbitrarily-chosen intervals given by the error bars.

3.5. Correlation analysis

We investigated whether the X-ray data of ISGRI correlate with the optical data of OMC. For this, investigation time intervals were specified during which the background-subtracted ISGRI count rates of Mrk 421 were lying in well-defined, but arbitrarily-chosen count-rate intervals. The average ISGRI count rates and the average optical fluxes of OMC were calculated for these time intervals. The result of this correlation analysis is shown in Fig. 9. Although the scatter of the results is quite large, a slight increase in the optical flux with increasing ISGRI count rate is detected. If one fits a straight line to the data, this dependence becomes more evident. The functional dependence of the OMC flux on the ISGRI rate is

$$F_{\rm OMC} = 2.5 \times 10^{-14} + 1.96 \times 10^{-16} \cdot R_{\rm IBIS}. \quad (7)$$

4. Results of spectral analysis

The results of a spectral analysis of the data of Mrk 421 at X-rays are presented in this section. First, we investigated how the energy spectrum evolves when going from the quiescent into the active state. Secondly, we calculated hardness ratios and looked for possible correlations. And third, we combined all data across the frequency range and constructed an energy-density spectrum νF_ν.

4.1. Spectral fits

The data from JEM-X and IBIS were collected for the quiescent and active states according to the times given in Table 3. Then different spectral models were fitted to the quiescent and active fluxes using the functions available in XSPEC11. Since ISGRI and JEM-X were excellently cross-calibrated by the two responsible teams, no cross-calibration factor had to be applied. The results of this fitting exercise are given in Tables 5 and 6. In addition, a spectrum with a log-parabolic function was fitted to the data (see Massaro et al. 2004). The results of these fits are shown in Table 7.

It turned out that a broken power law of the form

$$F(E) = A \cdot \left(\frac{E}{1\ \text{keV}}\right)^{-\alpha} \text{ for } E \le E_{\rm b} \quad (8)$$

$$F(E) = A \cdot E_{\rm b}^{\beta-\alpha} \cdot \left(\frac{E}{1\ \text{keV}}\right)^{-\beta} \text{ for } E > E_{\rm b} \quad (9)$$

(with A the normalization constant and with α and β the low- and high-energy spectral indices, respectively) gave the best fit result in both cases. (The joint power law gave an equally good fit, but

Table 5. Model fits to the JEM-X and ISGRI data of the quiescent state. The reference energy is 1 keV.

Model[a]	$\chi^2_{\rm red}$	normalization constant [keV^{-1} cm^{-2} s^{-1}]	α[b]	β[c]	$E_{\rm b}$ [keV][d]
power law (PL)	2.17	(0.378 ± 0.004)	2.318 ± 0.006	–	–
joint PL	1.85	$(9.3 \pm 3) \cdot 10^{-6}$	2.298 ± 0.007	6.5 ± 1.0	149 ± 11
broken PL	**1.83**	**(0.365 ± 0.005)**	**2.300 ± 0.006**	**3.0 ± 0.2**	**45 ± 4**
Band model	2.2	$(2.8 \pm 5) \cdot 10^{-5}$	2.0 ± 0.2	2.32 ± 0.01	13 ± 2
PL with exponential cutoff	2.17	(0.355 ± 0.006)	2.27 ± 0.01	–	311 ± 77

[a] The definitions of the mathematical forms of the used functions are contained in the XSPEC11 manual [with the exception of the joint PL which has the form $(\frac{E}{E_{\rm b}})^{-\alpha}/(1 + (\frac{E}{E_{\rm b}})^{\beta-\alpha})$].
[b] α is the spectral index at energies below $E_{\rm b}$.
[c] β is the spectral index at energies above $E_{\rm b}$.
[d] $E_{\rm b}$ is the break energy.

Table 6. Model fits to the JEM-X and ISGRI data of the active state. The reference energy is 1 keV. The parameters and functions have similar meaning to the one in Table 5.

Model	$\chi^2_{\rm red}$	normalization constant [keV^{-1} cm^{-2} s^{-1}]	α	β	$E_{\rm b}$ [keV]
power law (PL)	3.67	(0.530 ± 0.005)	2.164 ± 0.004	–	–
joint PL	1.85	$(9.9 \pm 3) \times 10^{-6}$	2.298 ± 0.007	6.65 ± 1.1	145 ± 10
broken PL	**1.89**	**(0.490 ± 0.005)**	**2.12 ± 0.05**	**2.90 ± 0.08**	**41 ± 2**
Band model	3.85	$(9 \pm 7) \times 10^{-5}$	1.81 ± 0.09	2.20 ± 0.02	23 ± 3
PL with exponential cutoff	2.36	(0.530 ± 0.005)	2.04 ± 0.01	–	132.0 ± 0.3

Table 7. Results of fits to the JEM-X and ISGRI data with a log-parabolic function $[=K \cdot (E/E_1)^{-a-b\cdot\log(E/E_1)}]$ for both states for a reference energy of $E_1 = 40$ keV.

State of source	$\chi^2_{\rm red}$	Normalization constant [keV^{-1} cm^{-2} s^{-1}]	a	b
quiescent	2.23	$(7.21 \pm 0.2) \times 10^{-5}$	2.35 ± 0.02	$(1.1 \pm 0.6) \times 10^{-2}$
active	2.91	$(1.77 \pm 0.03) \times 10^{-4}$	2.28 ± 0.01	$(5.0 \pm 0.5) \times 10^{-2}$

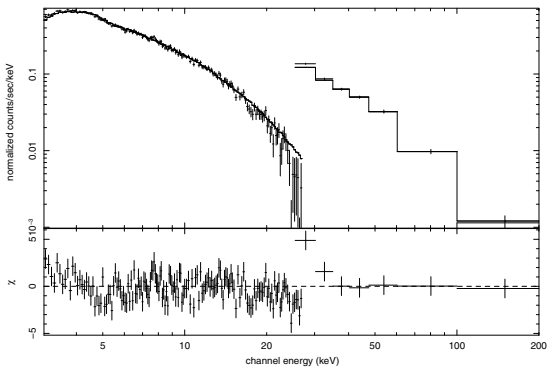

Fig. 10. Result of the fit of a broken power law to the JEM-X and ISGRI data in the quiescent state. *The top panel* shows the spectral data with the fit function, *the bottom panel* the residuals of the fit.

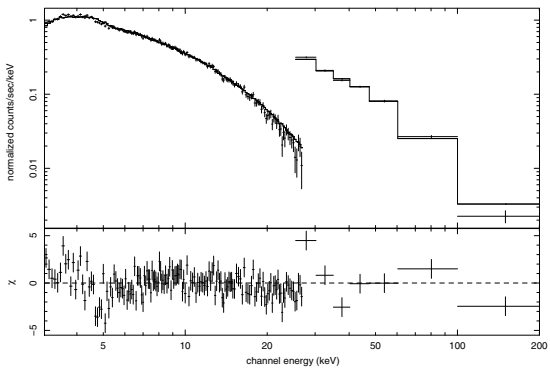

Fig. 11. Result of the fit of a broken power law to the JEM-X and ISGRI data in the active state. *The top panel* shows the spectral data with the fit function, *the bottom panel* shows the residuals of the fit.

it leads to an unrealistic high value of 6.5 for the high-energy power-law index β and was therefore discarded.)

The results of the fits for the quiescent and active states are shown in Figs. 10 and 11, respectively. With a reduced χ^2 value of ∼1.9, the fits are not excellent, but reasonable. The reason for the imperfect fit is that the fluxes of JEM-X and ISGRI in the overlapping energy intervals differ as is seen from the residuals. The results of the spectral analysis can be summarised as follows:

- a broken power law fits the data best in both cases (quiescent and active);
- the break energy $E_{\rm b}$ has a value of ∼43 keV;
- the index α is larger than 2;
- the spectral parameters do not change significantly with the state (although a slight spectral hardening of the low-energy index α is observed).

The third point indicates that we have only measured the declining part of the X-ray spectrum and can therefore not determine the maximum or minimum of the energy-density spectrum νF_ν. We can only say that the maximum is below the low-energy limit of JEM-X of 3 keV. It should be noted here that peak values up to 5.5 keV were measured with BeppoSAX (Massaro et al. 2004). The spectrum also falls off continuously to the upper

Table 8. Results of fits to the Swift-BAT data with a simple power law for both states for a reference energy of 1 keV.

State of source	$\chi^2_{\rm red}$	Normalization constant [keV^{-1} cm^{-2} s^{-1}]	α
quiescent	0.681	0.53 ± 0.2	2.46 ± 0.11
active	1.42	1.3 ± 0.4	2.49 ± 0.14

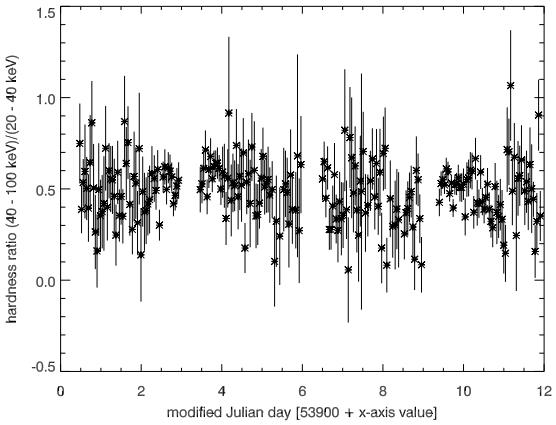

Fig. 12. Hardness ratio H/L as a function of time for the IBIS/ISGRI data.

energy limit of 200 keV, so a possible minimum of the νF_ν spectrum must lie at an energy greater than 200 keV.

The data from Swift-BAT were also spectrally analysed for the quiescent and the active state. They could be best fit with a simple power law. The results are summarised in Table 8. Within the errors, the spectral indices are identical for the quiescent and active states. This is consistent with the results of the data of Tables 5 and 6 for the joint power law where the spectral index also does not change with intensity. However, the spectral index obtained from the Swift-BAT data is with ∼2.5 somewhat larger than the one obtained from the JEM-X and IBIS/ISGRI data (∼2.3) but consistent with our result within 3σ.

The intensity of the Swift-BAT data between the quiescent and active states changes by a factor of 2.45 ± 1.2. This is a bit higher than the values derived from the results of Tables 5 and 6 but still compatible within the error.

4.2. X-ray luminosity

By integrating the broken power-law spectrum over the energies 3−200 keV and multiplying with the surface of a sphere one obtains the isotropic X-ray luminosity in this energy range. Using the parameters of Tables 5 and 6 one finds luminosities of 1.75×10^{45} erg/s and 3.73×10^{45} erg/s for the quiet and active states, respectively. This is much lower than the Eddington limit, which is in the range of $(2.4–9.6) \times 10^{46}$ erg/s. But it should be noted that the emission is actually beamed and that the luminosity is thus lower than given above.

4.3. Hardness ratios

We calculated the hardness ratio (HR) of the two IBIS/ISGRI energy bands 20−40 keV (L-band) and 40−100 keV (H-band) HR = H-band rate / L-band rate. It is plotted in Fig. 12 as a function of the time and in Figs. 13 and 14 as functions of the L-band and the H-band intensities. The hardness ratio in Fig. 12 is fairly constant in time and does not follow the lightcurves of

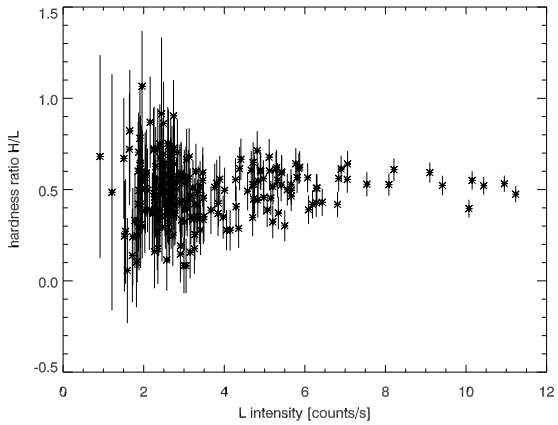

Fig. 13. Hardness ratio H/L as a function of the L-band (20−40 keV) intensity for the IBIS/ISGRI data.

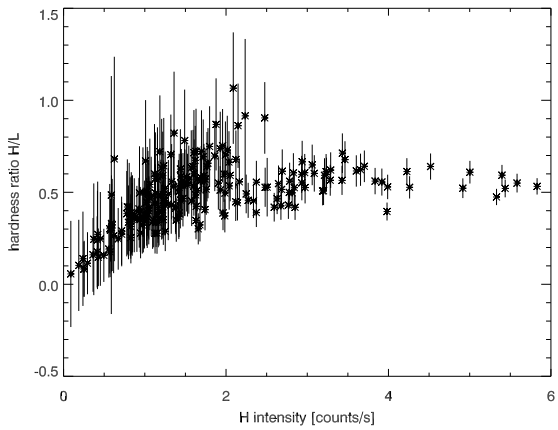

Fig. 14. Hardness ratio H/L as a function of the H-band (40−100 keV) intensity for the IBIS/ISGRI data.

Figs. 5 and 6, so we do not observe an evolution in the hardness ratio with intensity. When inspecting Figs. 13, 14, one notes a remarkable difference: whereas no correlation is obvious when one plots the ratios as a function of the L-band count rate (Fig. 13), a correlation for intensities up to ∼2 counts/s seems to be present when the plot is done as a function of the H-band count rate (Fig. 14). But this might be because there are no events with <1 counts/s in Fig. 13.

In Fig. 15 the hardness ratio is shown for two energy bands [(1−10 keV)/(0.3−1 keV)] of the Swift-XRT. A comparison with the lightcurve of Fig. 3 shows that the hardness ratio follows the lightcurve closely. This means that we have observed an intensity-hardness-ratio correlation; i.e., the brighter the source the harder the spectrum. But this is obviously not valid at all times. The last peak in Fig. 3 (at MJD ≈ 53 910.5) is only marginally visible in Fig. 15. One would expect a hardness ratio of ∼2 (similar to the hardness ratio observed at MJD ≈ 53909.5), but actually it is only about 1.5. This means that the emission process must have changed significantly on a time scale of <1 day. We obviously observed a clear hard-to-soft evolution.

The overall hardness-ratio correlation is also visible when one plots the Swift-XRT hardness ratio as a function of the Swift-XRT count rate as in Fig. 16. Although the positive correlation with the rate is not striking it is clearly recognisable. The large scatter around this correlation is probably due to a short-time scale and overlapping variability.

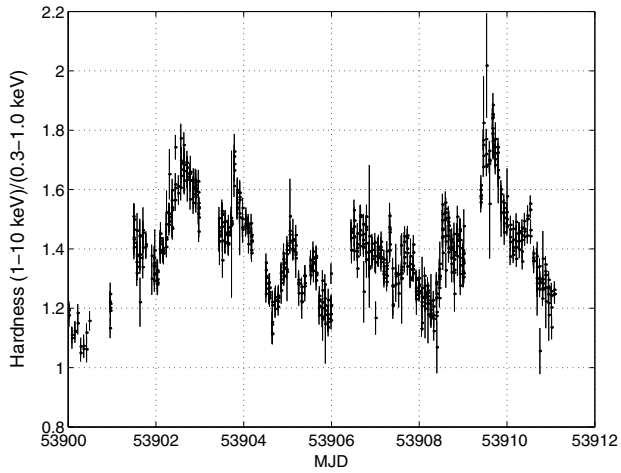

Fig. 15. Hardness ratio of the Swift-XRT data as a function of the time.

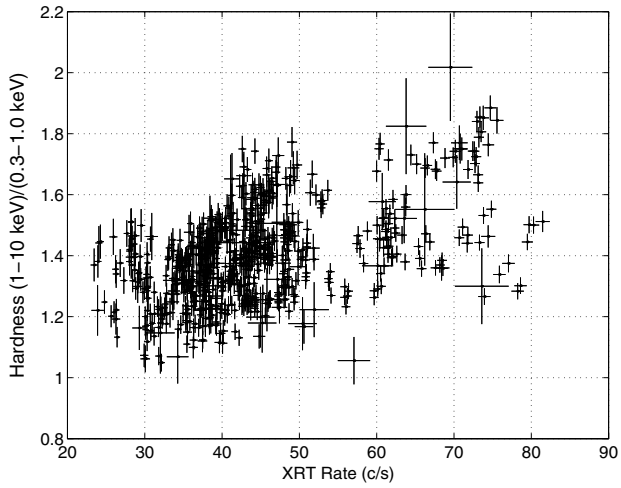

Fig. 16. Hardness ratio of the Swift-XRT data as a function of the XRT intensity.

4.4. Multiwavelength spectrum νF_ν

The data from all observations (with the exception of the JEM-X and ISGRI data) were averaged over the observation time span, corrected for extinction at optical wavelengths using the extinction value $E_{B-V} = 0.03$ of Burstein & Heiles (1982) and the formalism of Seaton (1979), converted to the same unit [erg/(cm^2 s)], and then plotted in an energy-density spectrum (νF_ν spectrum). This multiwavelength spectrum is shown in Fig. 17. Unfortunately the number of data points is sparse, especially at energies above ~500 keV where only two data points (measured at different times) at TeV energies exist. It should also be noted that the data used to create the average high state and low state SED data points shown in Fig. 17 were extracted from the same time windows for all instruments; however, the data are not strictly simultaneous. Due to this non-simultaneous data, it is possible that small time-scale flaring could cause a systematic offset of the SED from one energy band to another. This could explain the discrepancy between the Swift-XRT data and the JEM-X and IBIS data.

The data are compared with the theoretical models of Maraschi et al. (1999), Kino et al. (2002) and Blazejowski et al. (2005). The models of Maraschi et al. (1999) and Blazejowski et al. (2005) were adjusted to the flux measured by IBIS in the quiescent state by applying a factor of 3.2. Both models predict the actual flux measured by Whipple at TeV energies quite well, but seem to fail to fit the optical data and the radio flux. On the other hand, the model of Kino et al. (2002) fits the radio data quite well, but has problems fitting the X-ray and TeV data, together with the radio data. It is remarkable that the JEM-X spectrum is flatter than predicted by the models, even though their shape differs significantly. The three models also do not predict the break at an energy of 43 keV.

The best agreement between data and models is found for the model of Blazejowski et al. (2005). However, it should be noted here that the models were fitted to data measured at different times, so it is not surprising that they do not fit our data well. In contrast, they show that not only the intensity, but also the spectral shape of Mrk 421 is extremely variable.

4.5. Model fits

We also tried to fit a theoretical emission model to the data of the energy-density spectrum of Fig. 17. The model curves fitting the data shown in Fig. 18 best were obtained using a one-zone synchrotron self-Compton model (SSC) including the full Klein-Nishina cross section for inverse Compton scattering (Jones et al. 1968; Blumenthal et al. 1970). The model assumes a spherical blob with constant injection of non-thermal electrons and a constant escape rate for electrons and photons. The model details are described in Rüger et al. (2007).

In this calculation the electron distribution is assumed to be constanst (stationary) and is represented by a smoothed broken power law combined with an exponential cut-off as given in Tavecchio et al. (2001):

$$N(\gamma) = K\gamma^{-s_1}\left(1+\frac{\gamma}{\gamma_\mathrm{b}}\right)^{s_1-s_2}\exp\left(-\frac{\gamma}{\gamma_\mathrm{max}}\right) \tag{10}$$

with the differential electron number density N, Lorentz factor γ, break energy $E_\mathrm{b} = \gamma_\mathrm{b} mc^2$, spectral indices s_1 and s_2, normalization factor K, and cut-off energy γ_max. This phenomenological Ansatz for the spectrum is justified by self-consistent simulations (see Rüger et al. 2007).

With this electron distribution, the radiative transfer equation was solved numerically in the comoving frame and the observed spectrum obtained by applying the beaming effect using the Doppler-factor δ. Specifically, the transformation for the intensity is

$$I_{\nu,\mathrm{beamed}} = \delta^3\, I_{\nu,\mathrm{comovingframe}}. \tag{11}$$

In addition, one can show that, for dominating synchrotron losses, the second spectral index can be rewritten as $s_2 = s_1 + 1$, so one less parameter has to be determined. A first estimation of the parameter set is obtained by using the equations given in Kataoka et al. (2000). Small variations lead to the best-fit parameter set presented in Table 9.

From this table one can see that both parameter sets differ only in the break energy γ_b and the cut-off energy γ_max. The latter energy represents the efficiency of the acceleration mechanism. Since γ_b results from the emerging balance between cooling and acceleration of the electrons, a more efficient acceleration mechanism leads to both a higher γ_max and a higher γ_b. Therefore we conclude that the variability of the emission can be due to varying efficiency of the acceleration.

It should be noted, however, that a change in the spectrum of the injected electrons without changing the environmental parameters like the magnetic fields and/or the Doppler factor is difficult to understand. But the acceleration of particles can be

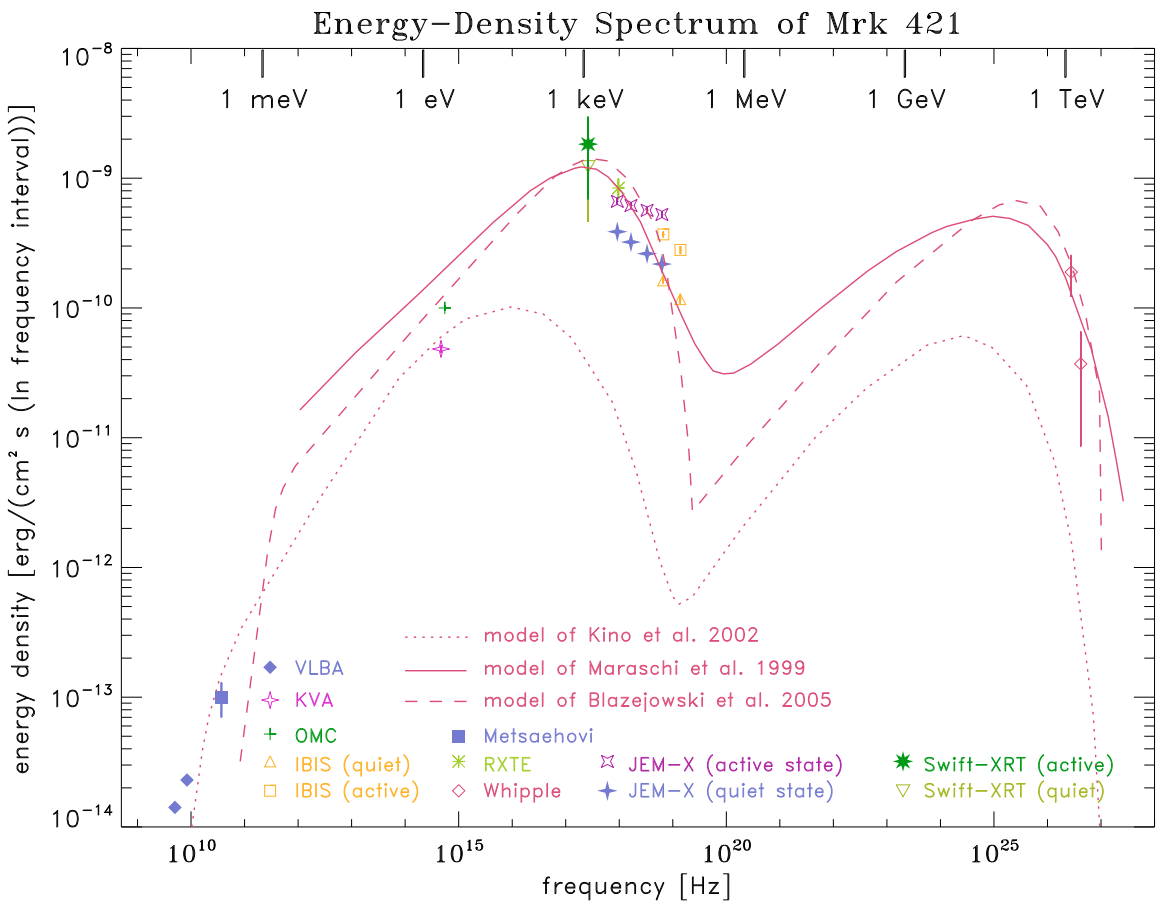

Fig. 17. The measured energy-density spectrum of Mrk 421 is compared with the three theoretical models of Maraschi et al. (1999), Kino et al. (2002), and Blazejowski et al. (2005). Please note that the data and the three models represent the source in different states and therefore reflect its spectral variability.

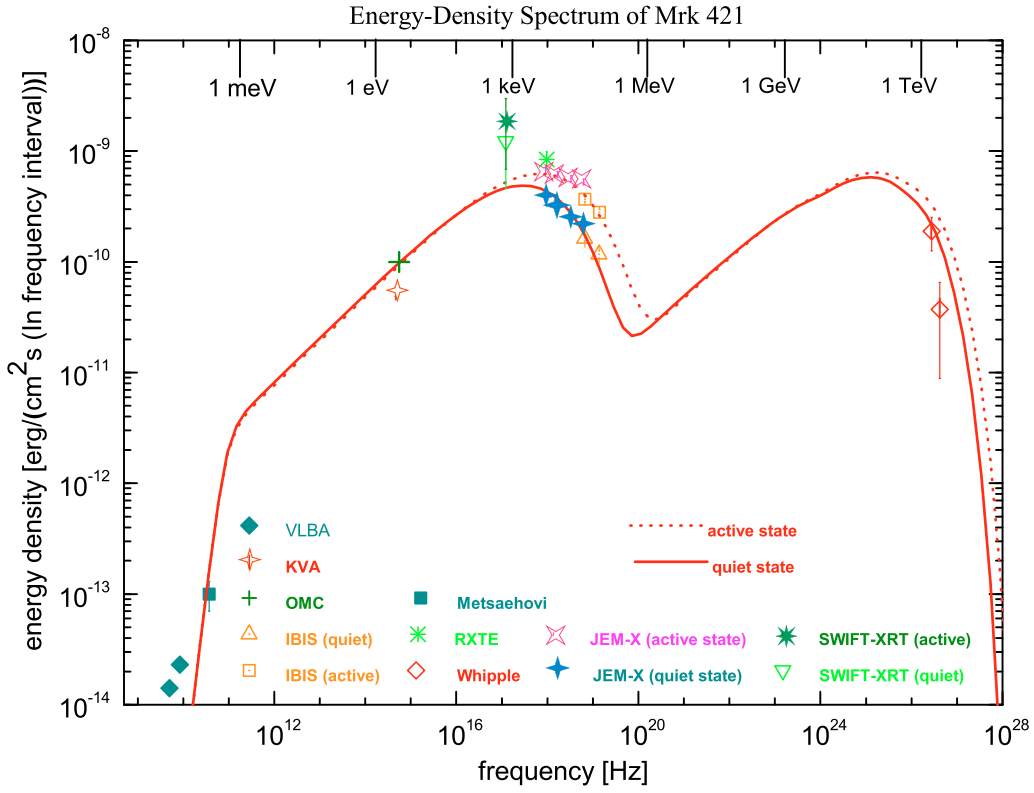

Fig. 18. The result of the model fits to the measured energy-density spectrum of Mrk 421.

Table 9. Best-fit parameters for high-state and low-state intensity when a one-zone synchrotron self-Compton model is fit to the spectrum.

Parameter	High-state	Low-state
γ_b	4×10^5	3×10^5
γ_{max}	1.2×10^6	7×10^5
s_1	2.2	2.2
s_2	3.2	3.2
B [G]	0.1	0.1
K [cm^{-3}]	1.6×10^4	1.6×10^4
δ	15	15

influenced without changing the environmental parameters by taking turbulence into account which can have a dramatic influence on the particle acceleration; on the one hand, enhanced turbulence can change the spectral indices (Vainio & Schlickeiser 1998; and Vainio & Spanier 2005), and on the other, the decay length of turbulence can change the maximum energy (Vainio & Schlickeiser 1998; and Vainio & Spanier 2005). However these effects are not covered in our model, just like the geometry of the shock and the shock thickness.

The fit presented here is not unique (see discussion in Tavecchio et al. 1998) and the observed change in spectral energy distribution can also be modelled by slightly varying the magnetic field strength and Doppler factor. The changes in these parameters would lead to a change in the electron spectrum, and such detailed modelling is beyond the scope of this paper. The Doppler factor and magnetic-field strength modelled here are similar to those derived for other TeV-emitting blazars. However, very long baseline interferometric observations show that such high Doppler factors would require very extreme assumptions for the viewing angle (0.015 degrees) and the Lorenz factor (25) (Piner & Edwards 2005). Therefore adopting models where the jet has a velocity structure (Georganopoulos & Kazanas 2003; Ghisellini et al. 2005) might be more feasible, but such modelling is beyond the scope of the paper.

5. Discussion and conclusions

The blazar Mrk 421 underwent an active phase in May/June 2006. INTEGRAL was therefore reoriented to observe this source for 12 days with the instruments OMC, JEM-X, and IBIS. Simultaneously the source was also observed by the Metsähovi and VLBA radiotelescopes, by the KVA telescope in the optical waveband, by RXTE and SWIFT at X-rays, and by Whipple at TeV energies. In X-rays, several strong flares were observed not seen at lower energies. Unfortunately the data at TeV energies are too sparse to allow such a conclusion for the high energies. In this context it is especially striking that the flares are not visible in the optical lightcurves, since it is thought that the X-rays and optical photons are produced by the same electron population via synchrotron emission. One would therefore expect similar lightcurves; but when fitting a theoretical one-zone synchrotron self-Compton model to the data, it is found that flares seen in X-rays may not necessarily be visible at lower frequencies.

However, other possibilities also exist for explaining the observed behaviour, rather than varying the efficiency of the acceleration. For example, it could be that the optical photons originate in larger emission regions and that the flares are thus occurring on longer time scales and are therefore smeared out. It could also be that the intensity fluctuations seen in X-ray are damped in the optical band. This view could be supported by the observed intensity correlation between OMC and IBIS in Fig. 9. Whereas the IBIS rate varies by a factor of ~5, the variation in the optical flux is only a few percent, so the high variations seen in X-rays are strongly damped in the optical range, hence barely visible. This could be achieved, for example, if the optical photons were obscured by some intervening clouds of matter that are transparent for the X-rays but not for the optical photons.

The spectral analysis of the JEM-X and IBIS/ISGRI data gave a surprising result: the spectral index α of the power law for the two states does not change much (from 2.12 to 2.3) at energies below 40 keV, although the intensity changes by factors up to 5. In the energy range 2−10 keV, Takahashi et al. (1996) found a clockwise evolution of the spectral index as a function of the intensity. But in their case the range of the change of the spectral index is nearly the same as reported by us (from 2.3 to 2.52), although the intensity only changes by a factor of 2. This shows that the observed slight hardening occurs predominantly at low intensities. This "saturation effect" is clearly seen in Fig. 14.

Another remarkable result is that the hardness ratio of the Swift-XRT data is strongly varying with intensity (see Fig. 15), whereas the hardness ratio of the IBIS/ISGRI data is more or less constant (see Fig. 12). This again shows that there is a conspicuous difference in the emission processes of the low- and high-energy X-rays. At energies <10 keV, the spectrum becomes harder with increasing intensity. This is not the case for X-rays with energies >20 keV. In the standard model in which the X-rays are produced by synchrotron radiation from the same electron population, this different behaviour is difficult to explain.

The picture becomes even more complex when one compares the lightcurves of Figs. 3 to 6. The two flares at the end of the observation interval (around MJD 53910) show a noticeable spectral difference: the first peak is much harder than the second one! If one assumes that each flare is produced by a relativistically-moving blob of electrons, the physical characteristics of each electron population and their environment (i.e. magnetic fields etc.) must be different, so the picture of jet emission is very complex and the extraction of the relevant information from the data requires a detailed and profound modelling of the emission processes.

Acknowledgements. We thank Tal Alexander for providing his program for the calculation of the ZDCF and for making his paper about this program available to us prior to publication. We also express our gratitude to Albert Domingo Garau who assisted us in analysing the OMC data correctly. A. Falcone and D. Morris acknowledge support from NASA contract NAS5-00136. Part of this work was supported by the "Ministerium für Bildung und Forschung" via the DLR under the grant 50.OG.9503.0. The Metsähovi team acknowledges the support from the Academy of Finland. The Very Long Baseline Array (VLBA) is a facility of the The National Radio-Astronomy Observatory (NRAO), which is operated by Associated Universities, Inc., under cooperative agreement with the National Science Foundation. We also thank an anonymous referee for her/his useful and valuable comments.

References

Aharonian, F. A. 2000, New Astron., 5, 377
Aharonian, F. A., Akhperjanian, A. G., Andronache, M., et al. 1999, A&A, 350, 757
Aharonian, F. A., Akhperjanian, A., Beilicke, M., et al. 2002, A&A, 393, 89
Aharonian, F. A., Akhperjanian, A., Beilicke, M., et al. 2003, A&A, 410, 813
Aharonian, F. A., Akhperjanian, A. G., Aye, K.-M., et al. 2005, A&A, 437, 95
Ajello, M., Greiner, J., Kanbach, G., et al. 2008, ApJ, 678, 102
Barth, A. J., Ho, L. C., & Sargent, W. L. W. 2003, ApJ, 583, 134
Barthelmy, S. D., Barbier, L. M., Cummings, J. R., et al. 2005, SSRv, 120, 143
Bessell, M. S. 1979, PASP, 91, 589

Blandford, R. D., & Rees, M. J. 1978, in Pittsburgh Conference on BL Lac Objects, ed. A. M. Wolfe, 328
Blazejowski, M., Blaylock, G., Bond, I. H., et al. 2005, ApJ, 630, 130
Bloom, S. D., & Marscher, A. P. 1996, ApJ, 630, 130
Blumenthal, G. R., & Gould, R. J. 1970, Rev. Mod. Phys., 42, 237
Brinkmann, W., Papadakis, I. E., Raeth, C., et al. 2005, A&A, 443, 397
Buckley, J. H., Akerlof, C. W., Biller, S., et al. 1996, ApJ, 472, L9
Burrows, D. N., Hill, J. E., Nousek, J. A., et al. 2005a, Space Sci. Rev., 120, 165
Burstein, D., & Heiles, C. 1982, AJ, 87, 1165
Catanese, M., Bradbury, S. M., Breslin, A. C., et al. 1997, ApJ, 487, L143
Charlot, P., Gabuzda, D. C., Sol, H., et al. 2006, A&A, 457, 455
Chiapetti, L., Maraschi, L., Tavecchio, F., et al. 1999, ApJ, 521, 552
Collmar, W., et al. 1999, Proc. of the 26th Int. Cosmic-Ray Conf., 3, 374
Cortina, J., et al. 2002, Proc. of the workshop, The Universe Viewed in Gamma Rays, Frontier Science Ser., 39, 261
Dermer, C. D., et al. 1992, ApJ, 630, 130
Edelson, R. A., & Krolik, J. H. 1988, ApJ, 333, 646
Falomo, R., Kotilainen, J. K., Treves, A., et al. 2002, ApJ, 569, L35
Fossati, G., Celotti, A., Chiaberge, M., et al. 2000, ApJ, 541, 153
Fossati, G., Buckley, J. H., Bond, I. H., et al. 2008, ApJ, 677, 906
Gaidos, J. A., Akerlof, C. W., Biller, S. D., et al. 1996, Nature, 383, 319
Gehrels, N., Chincarini, G., Giommi, P., et al. 2004, ApJ, 611, 1005
Georganopoulos, M., & Kazanas, D. 2003, ApJ, 594, L27
Ghisellini, G., & Maraschi, L. 1996, ASP Conf. Ser., 110, 436
Ghisellini, G., Maraschi, L., & Dondi, L. 1996, A&AS, 120, 503
Ghisellini, G., Tavecchio, F., & Chiaberge, M. 2005, A&A, 432, 401
Giebels, B., Dubus, G., & Khe'lifi, B. 2007, A&A, 462, 29
Hartman, R. C., Bertsch, D. L., Bloom, S. D., et al. 1999, ApJS, 123, 79
Henri, G., & Saugé, L. 2006, ApJ, 640, 185
Hillas, A. M., Akerlof, C. W., Biller, S. D., et al. 1998, ApJ, 503, 744
Horan, D., Badran, H. M., Bond, I. H., et al. 2002, ApJ, 571, 753
Jones, F. C., et al. 1968, Phys. Rev., 167, 1159
Kataoka, J. 2000, Ph.D. Thesis of University of Tokyo
Kataoka, J., Takahashi, T., Makino, F., et al. 2000, ApJ, 528, 243
Katarzynski, K., Sol, H., & Kus, A. 2003, A&A, 410, 101
Kazanas, D., Titarchuk, L. G., & Hua, X.-M. 1998, ApJ, 493, 708
Kerrick, A. D., Akerlof, C. W., Biller, S. D., et al. 1995, ApJ, 438, L59
Kildea, J., et al. 2007, Astropart. Phys., in press, http://dx.doi.org/10.1016/j.astropartphys.2007.05.004
Kino, M., Takahara, F., & Kusunose, M. 2002, ApJ, 564, 97
Kirsch, M. G. F., Briel, U. G., Burrows, D., et al. 2005, Proc. SPIE, 5898, ed. O. Siegmund, 22
Königl, A. 1981, ApJ, 243, 700
Konopelko, A., Mastichiadis, A., Kirk, J., et al. 2003, ApJ, 597, 851
Krawczynski, H., Sambruna, R., Kohnle, A., et al. 2001, ApJ, 559, 187
Krawczynski, H., Hughes, S. B., Horan, D., et al. 2004, ApJ, 601, 151
Krennrich, F., et al. 2003, Proc. of the 28th Int. Cosmic-Ray Conf., 5, 2603
Krennrich, F., Badran, H. M., Bond, I. H., et al. 2001, ApJ, 560, L45
Levine, A. M., Bradt, H., Cui, W., et al. 1996, ApJ, 469, L33
Lichti, G. G., Bottacini, E., Charlot, P., et al. 2007, Proc. of the 1st GLAST Symposium, AIP, 921, 371
Mannheim, K., et al. 1993, A&A, 269, 67
Maraschi, L., Fossati, G., Tavecchio, F., et al. 1999, ApJ, 526, L81
Massaro, E., Perri, M., Giommi, P., et al. 2004, A&A, 413, 489
Mastichiadis, A., & Kirk, J. G. 1997, A&A, 320, 19
Mücke, A., & Protheroe, R. J. 2000, Astropart. Phys., 15, 121
Mücke, A., Protheroe, R. J., Engel, R., et al. 2003, Astropart. Phys., 18, 593
Nilsson, K., Pasanen, M., Takalo, L. O., et al. 2007, A&A, 475, 199
Padovani, P., et al. 2007, Proc. of the 1st GLAST Symp. [arXiv:0704.0184v]
Piner, B. G., & Edwards, P. G. 2005, ApJ, 622, 168
Punch, M., Akerlof, C. W., Cawley, M. F., et al. 1992, Nature, 358, 477
Ravasio, M., Tagliaferri, G., Ghisellini, G., et al. 2004, A&A, 424, 841
Rebillot, P. F., Badran, H. M., Blaylock, G., et al. 2006, ApJ, 641, 740
Rüger, M., Spanier, F., & Mannheim, K. 2007, in preparation
Sambruna, R. M., Aharonian, F. A., Krawczynski, H., et al. 2000, ApJ, 538, 127
Seaton, M. J. 1979, MNRAS, 187, 73P
Sembay, S., Edelson, R., Markowitz, A., et al. 2002, ApJ, 574, 634
Sikora, M., Begelman, M. C., Rees, M. J., et al. 1994, ApJ, 421, 153
Takahashi, T., Tashiro, M., Madejski, G., et al. 1996, ApJ, 470, L89
Tal Alexander 2007, to be published
Tavecchio, F. 2005, Proc. of 10th Marcel Grossmann Meeting (MG10), ed. Novello, Perez-Bergliaffa, Ruffini (World Scientific)
Tavecchio, F., Maraschi, L., & Ghisellini, G. 1998, ApJ, 509, 608
Tavecchio, F., Maraschi, L., Pian, E., et al. 2001, ApJ, 554, 725
Teräsranta, H., Tornikoski, M., Mujunen, A., et al. 1998, A&AS, 132, 305
Treves, A., Carangelo, N., Falomo, R., et al. 2003, ASP Conf. Ser., 290, 621
Ulrich, M.-H., Maraschi, L., & Urry, C. M. 1997, ARA&A, 35, 445
Vainio, R., & Schlickeiser, R. 1998, A&A, 331, 793
Vainio, R., & Spanier, F. 2005, A&A, 437, 1
Villata, M., Raiteri, C. M., Lanteri, L., Sobrito, G., & Cavallone, M. 1998, A&AS, 130, 305
Wagner, R. 2007, http://www.mppmu.mpg.de/rwagner/sources/
Wamsteker, W. 1981, A&A, 97, 329